Haptic Force Feedback Enhances *de Novo* Learning of Arm Kinematics and Dynamics

Abbreviated title: Haptic Feedback Enhances *de Novo* Learning

Ian S. Howard[1*] and Laura Alvarez-Hidalgo[1]

[1]School of Engineering, Computing and Mathematics, University of Plymouth, Plymouth, United Kingdom.

*Correspondence should be sent to:
Ian S. Howard,
School of Engineering, Computing and Mathematics, University of Plymouth, Plymouth, United Kingdom.

Email: ian.howard@plymouth.ac.uk
Telephone: 0044 1752 586324

Keywords: De Novo, motor learning, bimanual, novel kinematics, 2D planar arm, dynamic learning,

Number of pages: 31
Number of figures: 4
Number of tables: 0
Number of words for Abstract: 231
Number of words for Introduction: 586
Number of words for Discussion: 1339

Conflict of Interest

The authors declare that they have no financial, personal, or professional interests that could be construed to have influenced the paper.

Acknowledgements

Support for ISH was provided by the School of Engineering, Computing and Mathematics, University of Plymouth. LAH was supported by a studentship from the EPSRC. We thank John Welsh for invaluable technical support. We thank David W. Franklin for useful scientific discussion. During the preparation of this work, the first author (ISH) utilized ChatGPT-4o for proofreading.

Significance Statement (109/120)

Humans can learn to control arbitrary extensions of the body. However, the factors that influence such de novo motor learning remain unclear. Here, we demonstrate that

haptic force feedback from a simulated endpoint mass enhances the acquisition of novel kinematic and dynamic mappings using a virtual arm. Participants who trained with haptic feedback showed greater adaptation to force fields and more accurate trajectory control. These results suggest that haptic input facilitates the formation of more efficient internal models during novel sensorimotor learning. In addition to their theoretical implications, these findings have practical implications for the use of haptic feedback during training for rehabilitation and the control of complex machinery.

Abstract (231/250)

The human motor system exhibits remarkable plasticity: not only can we master complex skills, but we can also learn to control artificial effectors. Here, we examine whether haptic force feedback from a simulated endpoint mass facilitates the de novo learning of novel kinematic and dynamic mappings. We investigate this using a virtual 2D planar arm controlled via a bimanual robotic manipulandum. Human participants moved two handles constrained to 1D channels, with handle positions specifying shoulder and elbow joint angles. Across two days, they performed center-out and out-back movements under two experimental conditions. On Day 1, one half of the participants practiced with a purely kinematic arm, whereas the other half received continuous haptic feedback from an endpoint mass. Although intrinsic hand movements were often initially sequential, participants rapidly adopted more coordinated control strategies, and trajectories became straighter with practice. Notably, the haptic-feedback group exhibited significantly greater improvements in virtual arm control. On Day 2, we introduced a velocity-dependent curl field to both groups. The curl field initially resulted in curved, loopy paths, but participants gradually compensated, consistent with internal-model formation. Prior exposure to haptic feedback conferred a superior capacity to adapt to the novel dynamics, evidenced by straighter trajectories and smaller directional biases throughout force-field exposure. These findings suggest haptic feedback enhances sensorimotor learning, possibly by engaging a distributed neural network of brain regions involved in motor skill acquisition and refinement.

Introduction (494/650)

People can master intricate motor skills, from rudimentary tool use to the operation of complex machinery [1–4]. Nevertheless, many motor control studies have examined relatively simple adaptations to altered task dynamics or visual feedback, which are often interpreted as recalibrations of the motor system. Many motor learning studies utilize veridical feedback from point-to-point movement tasks without kinematic transformations, with conclusions based on steady-state performance. For example, numerous studies have investigated both visuomotor adaptation [5–8] and dynamic learning tasks [9–12] across specific contexts.

Simultaneous adaptation to visuomotor and dynamic learning processes has also been investigated. For instance, participants can learn visuomotor rotations, viscous curl fields, or their combination within the same session [13], and evidence suggests that separate yet co-existing kinematic and dynamic internal models can be formed [14]. There has also been compelling research into more complex adaptations, such as

nonlinear visuomotor transformations that investigate movement in altered visual space [15], mirror reversal compensations [16], rotational adaptations [17], and sensorimotor transformations [18,19].

Mastering more complex remapping has also been investigated using finger motions to control the joint angles of a simulated planar two-link arm [20], demonstrating relevance to the effective control of prosthetic devices [20,21]. These studies have highlighted the pivotal role of visual feedback [21], in the learning of virtual object control through finger movements [22].

Skill acquisition that needs constructing entirely new mappings, rather than incrementally adjusting existing ones, is often referred to as "de novo" learning [23–25]. Such paradigms shift the focus from asymptotic performance levels to the mechanisms by which the motor system builds novel sensorimotor transformations capable of supporting arbitrary task spaces, Thus, whereas adaptation tasks primarily involve updating parameters within an existing internal model, de novo learning necessitates the establishment of entirely new sensorimotor mappings without reliance on prior control structures. Empirical evidence suggests that early phases of de novo learning are characterized by increased motor variability, reliance on cognitive strategies, and the gradual formation of stable control policies through trial-and-error exploration learning [24,25].

Here, we investigate "de novo" learning of novel kinematic and dynamic relationships using a virtual two-dimensional planar arm and the use of haptic feedback during learning. The arm was implemented using a bimanual robotic manipulandum. Participants controlled the simulated arm by moving two robotic handles backward and forward through two different one-dimensional channels. These hand movements directly controlled the angles of the shoulder and elbow joints, thereby determining the position of the end effector. Participants were tasked with performing center-out and out-back movements, allowing us to chart how practice refines their performance.

We examined two conditions: training with and without an endpoint mass attached to the end effector of the virtual 2D arm, to assess the impact of exposure to different dynamics on learning both novel kinematics and novel dynamics. In both scenarios, after participants became proficient at controlling the 2D arm, we evaluated their adaptation to the introduction of additional novel task dynamics, specifically a velocity-dependent viscous curl field.

Materials And Methods

Participants

We recruited 16 healthy, right handed human participants from a homogeneous demographic group and randomly allocated each participant to one of two experiments. All participants provided written informed consent, and the protocol was approved by the University of Plymouth's local ethics committee. All participants completed the Edinburgh Handedness Inventory [26] and the Quick Physical Activity Rating (QPAR) assessment [27].

Experiment 1 (Kinematic-Arm task) comprised eight participants (4 female, 4 male; mean ± SD age 20.8 ± 1.4 years; QPAR 40.9 ± 19.4).

Experiment 2 (Endpoint-Mass task) included eight participants (3 female, 5 male; mean ± SD age 21.9 ± 3.2 years; QPAR 46.3 ± 16.3).

To avoid experimental bias, participants were kept naïve to the study's hypotheses or objectives.

Experimental Setup

All experiments were conducted using two identical custom-built, back-drivable vBOT planar robotic manipulanda (Fig. 1A, B), which exhibits low mass at its handle [28]. Handle position was sampled with optical encoders at 500 Hz, and planar forces were updated by torque motors at the same rate. A planar virtual reality projection system was used to overlay images of targets, the end-effector cursor, and the 2D arm configuration in the plane of the vBOTs' movements. Participants were prevented from viewing their arms directly, were seated in front of the apparatus, and held one robot handle in each hand.

Two-joint Revolute Arm Simulation

We modelled a planar, two-joint (shoulder–elbow) revolute arm (Fig. 1C) centered at the workspace origin (0, 0).

The default arm configuration was purely kinematic and exhibited no intrinsic dynamics. Dynamics were introduced separately via a simulated 2kg endpoint mass and a velocity-dependent curl field. The shoulder joint was located at coordinates (–12, –2) cm, while both arm links were 12 cm in length and depicted as 2 mm-wide yellow lines. The shoulder and elbow joints were drawn as yellow circles with a radius of 0.5 cm. The end-effector position, located at the endpoint of the second arm segment, was drawn as a red circle with a radius of 0.5 cm.

Participants controlled the arm by moving the left and right handles on the vBOT manipulandum, which caused the arm to rotate around its shoulder and elbow joints, thereby controlling the location of its end effector. To accentuate the novelty of the mapping, handle positions and joint angles were deliberately decoupled from natural endpoint motion. Consequently, the arm movement directional mapping, represented by the parameter dir_{slider}, was set to –1, such that outward movements of the handles tended to generate inward movement of the cursor.

Mechanical Channels

The movement of the two vBOT handles were restricted to linear channels along the y-axis, with a length parameter (*chanLen*) of 30 cm. To spatially separate the hands, the left and right channels were offset from the center of the workspace by ±10 cm, yielding central handle positions of (-10, 0) cm and (+10, 0) cm, respectively.

To constrain each handle to a single degree of freedom, mechanical channels were used perpendicular to the permitted y-direction of motion [29], with a stiffness of k_{chan} = 4,000 N/m and a damping coefficient b_{chan} = 30 N.s/m. The channels were implemented according to the following equation, which relates the forces experienced at a given handle $[F_{xh} \quad F_{yh}]^T$ to its position $[x_h \quad y_h]^T$ and velocity $[\dot{x}_h \quad \dot{y}_h]^T$:

$$\begin{bmatrix} F_{xh} \\ F_{yh} \end{bmatrix} = k_{chan} \begin{bmatrix} -1 & 0 \\ 0 & 0 \end{bmatrix} \begin{bmatrix} x_h \\ y_h \end{bmatrix} + b_{chan} \begin{bmatrix} -1 & 0 \\ 0 & 0 \end{bmatrix} \begin{bmatrix} \dot{x}_h \\ \dot{y}_h \end{bmatrix} \tag{1}$$

Control of the Simulated Arm

The y-position (y) of each handle was mapped to the corresponding joint angle (θ) using a linear scaling:

$$\theta = \theta_{min} + (\theta_{max} - \theta_{min}) \frac{\left(dir_{slider} \cdot y + \frac{\text{chanLen}}{2}\right)}{\text{chanLen}} \tag{2}$$

The y-location of the left handle y_{h1} was mapped to a joint angle θ_1 between the range of $\theta_{min} = 0$ radians and $\theta_{max} = \pi$ radians:

$$\theta_1 = \frac{(15 - y_{h1})}{30}\pi \tag{3}$$

The y-location of the right handle y_{h2} was mapped to a joint angle θ_2, between the range of $\theta_{min} = -\pi$ radians and $\theta_{max} = 0$ radians:

$$\theta_2 = \frac{(15 - y_{h2})}{30}\pi - \pi \tag{4}$$

Differentiating equations (2) and (3) results in a mapping between the handles' y-velocities and the corresponding joint angular velocities:

$$\begin{bmatrix} \dot{\theta}_1 \\ \dot{\theta}_2 \end{bmatrix} = -\frac{\pi}{30} \begin{bmatrix} \dot{y}_{h1} \\ \dot{y}_{h2} \end{bmatrix} \tag{5}$$

Simulating Forward Kinematics

Forward kinematics of the 2D arm is necessary to calculate the endpoint position and visualize its configuration. By trigonometric analysis (Fig. 1C), the positions of the elbow and end effector in Cartesian extrinsic coordinates can be expressed using matrix equations:

$$\begin{bmatrix} x_{elbow} \\ y_{elbow} \end{bmatrix} = \begin{bmatrix} l_1 \cos(\theta_1) \\ l_1 \sin(\theta_1) \end{bmatrix} + \begin{bmatrix} x_{shoulder} \\ y_{shoulder} \end{bmatrix} \tag{6}$$

$$\begin{bmatrix} x_{end} \\ y_{end} \end{bmatrix} = \begin{bmatrix} l_1 \cos(\theta_1) + l_2 \cos(\theta_1 + \theta_2) \\ l_1 \sin(\theta_1) + l_2 \sin(\theta_1 + \theta_2) \end{bmatrix} + \begin{bmatrix} x_{shoulder} \\ y_{shoulder} \end{bmatrix} \tag{7}$$

Differential kinematics of the 2D arm are needed to relate handle velocities to arm endpoint velocities and to relate endpoint forces back to the forces experienced at the control handles of the vBOTs. The Jacobian matrix of the 2D arm is given as:

$$J = \begin{bmatrix} \frac{\partial x_{end}}{\partial \theta_1} & \frac{\partial x_{end}}{\partial \theta_2} \\ \frac{\partial y_{end}}{\partial \theta_1} & \frac{\partial y_{end}}{\partial \theta_2} \end{bmatrix} = \begin{bmatrix} -l_1 \sin(\theta_1) - l_2 \sin(\theta_1 + \theta_2) & -l_2 \sin(\theta_1 + \theta_2) \\ l_1 \cos(\theta_1) + l_2 \cos(\theta_1 + \theta_2) & l_2 \cos(\theta_1 + \theta_2) \end{bmatrix} \tag{8}$$

The relationship between the handle velocities and the extrinsic endpoint velocity is given by:

$$\begin{bmatrix} \dot{x}_{end} \\ \dot{y}_{end} \end{bmatrix} = J \begin{bmatrix} \dot{\theta}_1 \\ \dot{\theta}_2 \end{bmatrix} = -\frac{\pi}{30} J \begin{bmatrix} \dot{y}_{h1} \\ \dot{y}_{h2} \end{bmatrix} \tag{9}$$

Task Force Feedback

Although the arm itself was modeled as a purely kinematic structure with no intrinsic dynamics, other endpoint dynamic environments could be simulated by relating the load at the endpoint back to the y-direction forces experienced by the participants at the control handles. The relationship between the virtual arm endpoint force vector $[F_{xend} \quad F_{yend}]^T$ and the joint torque vector $[\tau_1 \quad \tau_2]^T$ is given by:

$$\begin{bmatrix} \tau_1 \\ \tau_2 \end{bmatrix} = J^T \begin{bmatrix} F_{xend} \\ F_{yend} \end{bmatrix} \tag{10}$$

Where J^T is the transpose of the arm's Jacobian matrix. The torques $[\tau_1 \quad \tau_2]^T$ at the arm joints are mapped to corresponding y-direction forces $[F_{h1} \quad F_{h2}]^T$ applied at the vBOT handles by accounting for the mechanical advantage relationship between the handle displacement and the joint rotational angles. This yields the following conversion formula:

$$\begin{bmatrix} F_{h1} \\ F_{h2} \end{bmatrix} = dir_{slider} \frac{(\theta_{max} - \theta_{min})}{\text{chanLen}} \begin{bmatrix} \tau_1 \\ \tau_2 \end{bmatrix} \tag{11}$$

Substituting in the expression for joint torques, and numeric values, this leads to the final expression for the force along the y-axis at the handle in terms of endpoint force:

$$\begin{bmatrix} F_{h1} \\ F_{h2} \end{bmatrix} = -\frac{\pi}{30} J^T \begin{bmatrix} F_{xend} \\ F_{yend} \end{bmatrix} \tag{12}$$

Endpoint Dynamics Simulation

In the null-field condition, when the arm endpoint was unloaded, no endpoint forces were present, and no endpoint forces were experienced at the control handles during arm movement. When endpoint dynamics were introduced, namely, a viscous curl field, added mass, or the combination of both, the endpoint forces arising from these dynamics were mapped back to the handles and experienced by the participants as they moved the arm around the workspace.

Endpoint Curl Field Simulation

In curl field endpoint trials, a velocity-dependent curl field [12], was implemented using the relationship between arm endpoint velocity and the endpoint force:

$$\begin{bmatrix} F_{xend} \\ F_{yend} \end{bmatrix} = b_{curl} \begin{bmatrix} 0 & -1 \\ 1 & 0 \end{bmatrix} \begin{bmatrix} \dot{x}_{end} \\ \dot{y}_{end} \end{bmatrix} \tag{13}$$

The curl field viscous field constant, b_{curl}, was set to ±16 N.s/m, where the sign determined the direction of force field (clockwise or counterclockwise). In each experiment, the curl field direction was counterbalanced across all the eight participants to minimize the effect of directional bias on behavior. Each participant experienced only a single curl field direction.

The endpoint velocity used in Equation (13) was calculated from the handle velocities using Equation (9). The corresponding forces experienced in the y-direction at the handles were then calculated using Equation (12). The total 2D force applied to the vBOT handles corresponds to the sum of the channel force component and the force feedback component arising from the effect of the curl field.

Simulating Endpoint Mass

To achieve a stable simulation, a moving mass was modeled as connected to the endpoint of the virtual arm by a strong spring. In addition, viscous damping was included in the simulation, to improve stability,

At the start of the simulation, the spring was set to its rest length, and the mass position was initialized at the current endpoint of the arm.

$$\begin{bmatrix} x_m \\ y_m \end{bmatrix} = \begin{bmatrix} x_{end} \\ y_{end} \end{bmatrix} \tag{14}$$

We set the velocity of the mass and its initial acceleration to zero.

$$\begin{bmatrix} v_{xm} \\ v_{ym} \end{bmatrix} = \begin{bmatrix} 0 \\ 0 \end{bmatrix} \tag{15}$$

$$\begin{bmatrix} a_{xm} \\ a_{ym} \end{bmatrix} = \begin{bmatrix} 0 \\ 0 \end{bmatrix} \tag{16}$$

We also set the force acting on the mass to zero.

$$\begin{bmatrix} F_{xm} \\ F_{ym} \end{bmatrix} = \begin{bmatrix} 0 \\ 0 \end{bmatrix} \tag{17}$$

In the main simulation update loop, running at the nominal frequency of 1kHz, the real-time simulation of the arm and endpoint mass is then carried out. At each time step, Euler integration was used to update the position of the mass.

$$\begin{bmatrix} x_m \\ y_m \end{bmatrix} = \begin{bmatrix} x_m \\ y_m \end{bmatrix} + \begin{bmatrix} v_{xm} \\ v_{ym} \end{bmatrix} \Delta\mathrm{t} \tag{18}$$

Where $\Delta\mathrm{t}$ is the actual timestep since the previous update (nominally 1ms). We then estimate acceleration of the mass using the equation:

$$\begin{bmatrix} a_m \\ a_m \end{bmatrix} = \frac{1}{m} \begin{bmatrix} F_{xm} \\ F_{ym} \end{bmatrix} \tag{19}$$

Where m is the mass at the point (2 kg) and $[F_{xm} \quad F_{ym}]^T$ is the force acting on the mass. We use Euler integration of the acceleration of the mass to calculate mass velocity:

$$\begin{bmatrix} v_{xm} \\ v_{ym} \end{bmatrix} = \begin{bmatrix} v_{xm} \\ v_{ym} \end{bmatrix} + \begin{bmatrix} a_{xm} \\ a_{ym} \end{bmatrix} \Delta\mathrm{t} \tag{20}$$

The force acting on the mass was then estimated by consideration of the extension of the spring, with spring constant k_{mass} = 2000 N/m, connecting the endpoint mass to the endpoint of the arm:

$$\begin{bmatrix} F_{xm} \\ F_{ym} \end{bmatrix} = -k_{mass} \left(\begin{bmatrix} x_m \\ y_m \end{bmatrix} - \begin{bmatrix} x_{end} \\ y_{end} \end{bmatrix} \right) \tag{21}$$

An additional viscous damping term was applied to the endpoint to improve stability:

$$\begin{bmatrix} F_{xdamp} \\ F_{ydamp} \end{bmatrix} = -b_{end} \begin{bmatrix} \dot{x}_{end} \\ \dot{y}_{end} \end{bmatrix} \tag{22}$$

Where damping viscosity b_{end} = 10 N.s/m. The mass force (Equation 21) and damping force (Equation 22) were summed together and the corresponding forces experienced in the y-direction at the handles were then calculated using Equation (12). Again, the total 2D force applied to the vBOT handles corresponds to the sum of the channel force component and the force feedback endpoint components.

Simultaneous Endpoint Mass and Curl Field

In trials with both endpoint mass and a curl field present, we first calculate the endpoint mass and curl field components as described previously. The vBOT applies an overall 2D force to its handles by summing the force-feedback components from the curl field and the endpoint mass, along with the additional channel forces that restrict handle movement to the y-direction.

Experimental Protocol

Participants executed center-out and out-center reaching movements with the endpoint of the two-dimensional (2D) planar arm. Each center-out movement began at a central 'home' position (radius: 1.0 cm, pink) and ended at one of eight pseudorandomly selected peripheral targets (radius: 1.0 cm, pink), evenly spaced (0°, 45°, 90°, 135°, 180°, 225°, 270°, and 315°) on a 10 cm-radius circle centered at (0, 0). The home start position was in the mid-sagittal plane, approximately 30 cm below eye level and 30 cm in front of the participant's chest. An out-center movement then followed, which involved reaching back from the previous center-out target to the central home start position.

At the beginning of each trial, the manipulanda automatically positioned the handles so the endpoint of the virtual arm was at the home location. Participants were required to keep the cursor within the central starting position and maintain cursor speed below 0.1 cm/s. After a 0.5 s delay, a target appeared at a pseudo-randomly selected location, the arm became visible, and a tone indicated that the participant should move out to the target.

Each block comprised 17 trials: 8 outward and 8 inward movements with the simulated arm visible. In addition, there was one outward movement where the arm was not visible. The outward movements constituted a typical center-out task, enabling comparison of behaviors with other such studies in the literature. The inward (return-to-home) movement provided further coverage of the operating space using movements in the opposite direction. A trial terminated when the cursor was within 0.5cm of the target and cursor speed had dropped below 0.01 cm/s.

An outward catch trial movement to a randomly selected target from one of the four cardinal directions (0°, 90°, 180°, or 270°) was also included in each block of 17 trials. In this catch trial, both the arm and the endpoint cursor location were invisible, allowing assessment of feedforward control. Since catch trials are made without visual indication of cursor position, trial termination only occurs when cursor movement speed dropped below 0.01 cm/s, since initially accurate movement to a target is difficult and could not be guaranteed.

Participants were required to complete the movement within 10 seconds; otherwise, the trial was aborted. During each trial, the curl field within the channels and the virtual arm's endpoint location were recorded.

Experiments

We conducted two independent experiments, each comprising eight randomly assigned participants, to investigate the learning and control of a virtual planar (2-D) arm. Each participant completed two sessions of 2,380 trials on separate days (see Fig. 1H).

Kinematic Arm Task Experiment 1.

This experiment examined de novo acquisition of kinematic control of a two-dimensional arm operating without endpoint mass. On Day 1, participants executed point-to-point reaches, in a null-force environment.

Day 2 began with a brief re-exposure to the null field, comprising the first 20% of trials (n = 476), to re-establish baseline performance. A velocity-dependent viscous curl field was then imposed for the majority of the session (n = 1,870). The resulting endpoint forces were computed as joint torques via the Jacobian transpose and subsequently transformed into linear forces at the handles, enabling participants to perceive the perturbation directly. In the final two blocks (n = 34 trials) the curl field was removed to assess wash-out after-effects of the prior dynamic exposure.

Endpoint Mass Arm Task Experiment 2.

Experiment 2 was similar to Experiment 1, but introduced a constant 2 kg endpoint mass, thereby providing continuous haptic load feedback. The actuation forces generated by moving the mass were related to the virtual arm joint torques, and subsequently mapped to forces at the control handles.

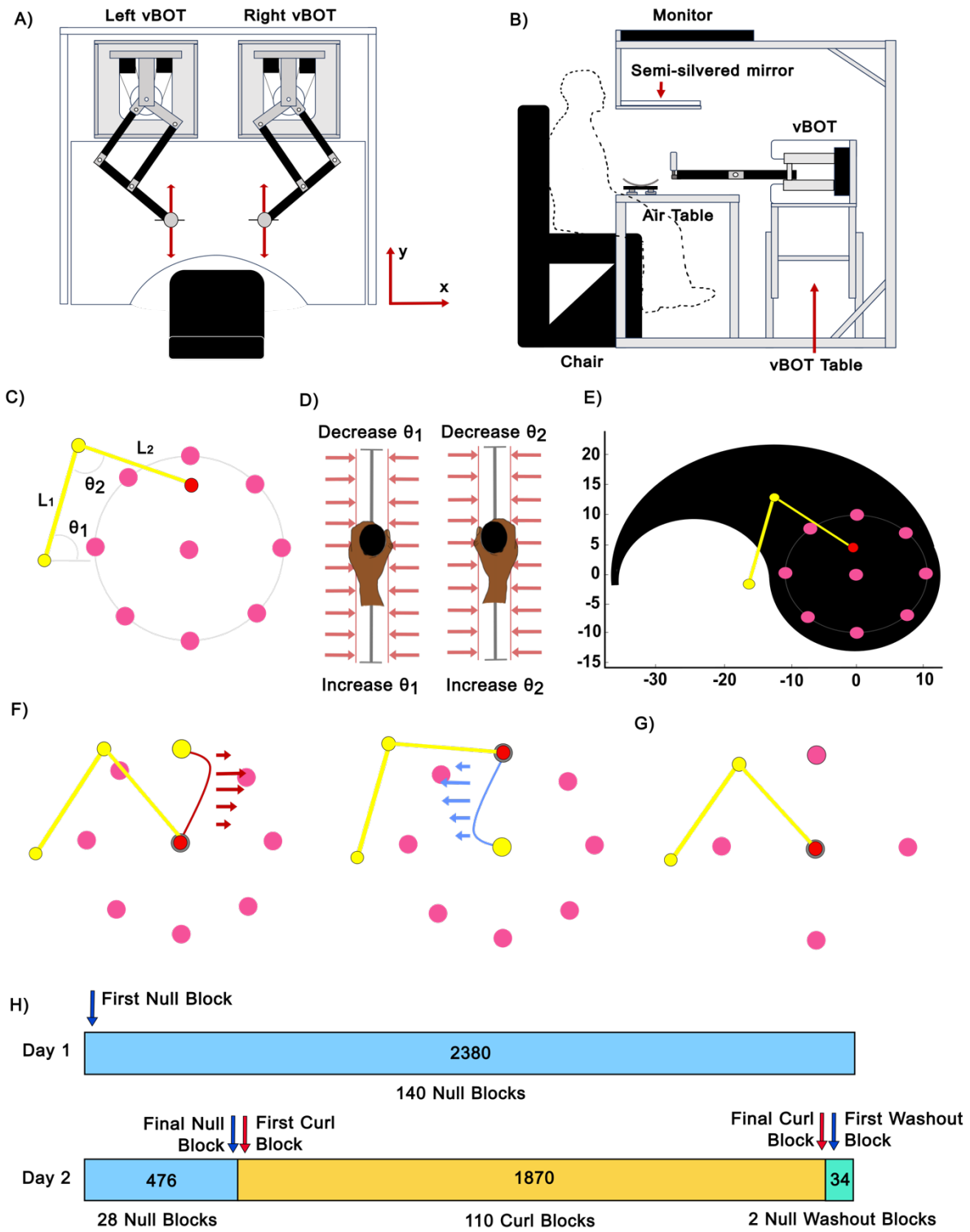

Figure 1. Experimental Set-Up and Task Design. **A:** Control of a virtual 2D arm was conducted using the vBOT robotic manipulandum. **B:** The left and right handle y-positions determine the arm joint angles. The handles are constrained to linear channels. **C:** Plan view of the simulated planar two-joint revolute arm. The lower link has a length L_1, and the upper link has a length L_2. The position of the end effector is affected by both link angles θ_1 and θ_2. **D:** Angles θ_1 and θ_2 are controlled by moving the robotic handles in two separate channel trials. Moving the left handle (controlling θ_1) up decreases the angle; while moving it down increases the angle. Similarly,

moving the right handle (controlling θ_2) up decreases the angle, and moving it down increases it. **E:** Workspace of the simulated 2D arm is shown in black. A center-out and out-back task, home position and targets fit within the workspace. **F:** Curl field trials. Participants performed outward and inward movements toward a displayed yellow target. After completing the training, they were exposed to two distinct directional curl fields. Half of the participants experienced clockwise (CW) curl fields during outward movements and inward movements. The other half experienced counterclockwise (CCW) curl fields during outward and inward movements. This design counterbalanced the exposure to each field type across participants. **G:** Channel trials. These only used a single adaptation movement direction to a target point (0°, 90°, 180°, or 270°). **H:** Training and testing trial schedule for the experiment. Each block contains 17 trials: 8 cursor-visible center-out movements to a target, 8 cursor-visible out-back movements to the home position, and 1 invisible-cursor center-out catch movement to one of four targets. **I**. Location of informative trajectory observation points: First Null Block, Final Null Block, First Curl Block, Final Curl Block, and First Washout Block.

Data Analysis

The experimental data were processed offline using MATLAB R2024a.

Hand Trajectory Plots

Hand trajectory plots provide an intuitive visualization of participants' movement behavior throughout the experiment. They illustrate naïve control early in training, the progressive refinement that accompanies exposure to external dynamics (e.g., viscous curl fields), and the re-emergence of baseline patterns once those forces are removed, thereby revealing learning, adaptation, and de-adaptation in a single display.

In both experiments, several key phases are critical to understanding participants' motor performance and adaptation. These include the first and last blocks of null-field trials (baseline establishment and improvement), the first and last blocks of curl-field exposure (early and late adaptation), and the first wash-out block (de-adaptation).

Hand trajectory plots allow direct comparison of movements during outward and inward paths and provide insight into both extrinsic trajectories (hand paths in Cartesian space) and intrinsic trajectories (joint space paths). Additionally, catch trials—in which the target is shown but no visual feedback of the arm is provided—are included to assess predictive adaptation to the control of the novel kinematics.

Trajectory quantification: Several measures were calculated to quantify the movement trajectory of each individual trial. First, the movement start, and end points were determined in both time and space. A movement was considered to have started when the center of the extrinsic cursor location left the center of the starting target circle (radius: 0.5 cm) and was traveling at a speed greater than 0.01 cm/s. A movement was considered to have stopped when the center of the extrinsic cursor reached the extrinsic target circle (radius: 0.5 cm).

Performance Metrics

We quantified kinematic accuracy with four complementary deviation metrics including two temporal-spatial measures.

Extrinsic Absolute Maximum Perpendicular Error (AMPE): For each trial we took the absolute value of the maximum perpendicular deviation of the 2D arm endpoint trajectory from the ideal straight-line joining the start cursor location and the target cursor location in extrinsic space. This measure ensures that positive and negative deviations over trials do not cancel out and gives an overall indication of how well participants were able to move in a straight trajectory from the starting point to the target, making it a suitable metric to quantify how well participants could control the virtual arm.

Extrinsic Signed Maximum Perpendicular Error (SMPE): We also retained the signed maximum deviation of the 2D arm endpoint trajectory from a straight-line path, between the starting cursor location and the target cursor location in extrinsic space, was calculated. This measure preserved the direction of the maximum deviation from a straight-line trajectory. Consequently, the effects of random fluctuations are minimized, since contributions from positive and negative deviations cancel out in the averaging procedure. As such, since its introduction, this is typically the preferred metric used to assess deviation from a straight line in curl field adaptation experiments [30].

Movement Duration: Difference between movement onset and termination times.

Movement Length: To estimate the extrinsic movement path length, we computed the sum of the distances between adjacent (x, y) cursor trajectory positions, calculated using the Pythagorean theorem, from the start to the end movement locations.

Mean ± SE over Trials and Participants

The average values of each trajectory metric was first computed across all trials within a given set of blocks. The mean ± standard errors (SE) of the resulting average values were then calculated across all participants.

Using signed Maximum Perpendicular Error (SMPE) values allows positive and negative deviations from straight paths to cancel each other out, a phenomenon that does not occur when averaging absolute measures of MPE. Consequently, the group-mean signed MPE is a clearer indicator of systematic bias in the trajectories and is especially insightful in analyzing trajectories to examine the effect of curl field exposure.

Statistics

Statistical analyses were conducted in JASP 0.19.1 [31]. A Mauchly test was applied to check for sphericity wherever applicable. In cases where the Mauchly test was significant, the degrees of freedom were adjusted using a Greenhouse-Geisser

correction. The α-level was set to 0.05 in all tests. We report omega squared as the effect size (ω^2).

Each of the two experiments was conducted with different participants, resulting in a total of two sets of AMPE, SMPE, path length and movement duration data. For each of these two datasets in isolation, we first performed repeated measures ANOVAs to examine differences in AMPE, SMPE, path length and duration data at various critical phases within each experimental condition.

To evaluate the four metrics within each experimental condition, we compared the mean of each metric over two blocks for the initial null phase, the final null phase, the initial curl field exposure phase, the final curl field exposure phase, and the washout phase. This comparison was conducted using a repeated-measures ANOVA, with phase as a repeated-measures factor (5 levels). When a significant main effect was observed, we proceeded with post-hoc comparisons using the Holm-Bonferroni correction.

To compare results across experiments for the four metrics, we compared the mean of each metric over ten blocks using an ANOVA between the final null phase, the initial curl field exposure phase, and the final curl field exposure phase. In this analysis, experimental condition (2 levels) was considered the factor. Post-hoc comparisons were conducted with the Holm-Bonferroni correction if a significant main effect was detected

Results

The Kinematic Arm Task Experiment 1 involved first learning how to control a virtual revolute arm using a purely arbitrary kinematic mapping between hand movements to its joint angles and then investigated the effect of an endpoint curl field. Each participant performed two sets of 2380 trials on separate days. On Day 1, the arm was controlled with a purely kinematic mapping from hand positions to joint angles. On Day 2, the first 20% of trials maintained this kinematic mapping. For the remainder, the endpoint was simulated moving through a viscous curl field and participants experienced its corresponding joint torques as reaction forces at their hands.

We recorded and subsequently analyzed, the behavior of participants as they learned the novel kinematics and dynamics of the simulated 2D arm. This process was undertaken for both experiments, Experiment 1 – Null Field Task and Experiment 2 – Endpoint Mass Task. See Fig. 1H for the location of the critical informative phases in the experiments discussed below.

Trajectory Plots Kinematic Arm Task Experiment 1

We first examined the representative hand trajectories during the initial null phase for a single participant. Fig. 2A shows the extrinsic and corresponding intrinsic outward-movement trajectories for the first null block for a typical participant. The extrinsic paths were highly erratic as participants searched for the target location, and the corresponding intrinsic movement trajectories show typical segmented and

independent hand movements seen as participants learned to control the 2D arm. By the final null block, the participant exhibited straighter extrinsic paths, as shown in Fig. 2B. The previously independent hand movements were replaced by simultaneous, continuous intrinsic motions.

We then examined outward movement trajectory trends across participants. Fig. 2C plots the mean ± SE extrinsic trajectories across half the participants in the clockwise (CW) condition, and Fig. 2D shows the corresponding trajectories in the counterclockwise (CCW) condition. In the initial null block, trajectories deviated substantially from straight-line paths. However, by the end of the null phase, their outward paths to the targets became consistently much straighter. Upon introducing a curl field, participants' hand trajectories became systematically curved, as the force field pushed them away from their straight paths. By the end of the curl field exposure phase, participants exhibited adaptation to the curl field, straightening their hand trajectories. This adaptation process resembles the typical behavior observed in curl field learning. In the final washout phase, the curl field was removed, and pronounced after-effects were observed. These after-effects manifested as deviations from the intended path, in the direction opposite to the original curl field force.

We examined the mean ± SE speed profiles across all extrinsic movements over the same experimental phases, as shown in Fig. 2E. Initially, movements were slow and exhibited a similarly low speed across the movement trajectory. By the end of the null phase, the speed profile more closely resembled that of a minimum-jerk extrinsic point-to-point movement profile, exhibiting a characteristic peak. However, there was still some asymmetry in the speed profile. The introduction of the curl field slowed down the movements and skewed the profile toward lower speeds as well, although the shape of the speed profile became more symmetric and faster by the end of adaptation to the curl fields. In the washout phase, the after-effect led to a somewhat more erratic speed profile.

Catch trials, performed without visual feedback, assessed feedforward control of the virtual arm. We examined the catch trial trajectories made by participants at the start of the experiment, at the end of the null exposure phase, and at the end of curl field exposure. The raw trajectories are presented in Fig. 2F, as each participant behaved differently, and average plots would lose their individual characteristics. Initially, the movements were often made in inappropriate directions and of inappropriate length. By the end of the null training, movement directions and lengths had improved, although there was still inaccuracy in most of the trajectories. At the end of curl field training, by which time participants had the most experience learning to control the virtual arm, the directions and lengths of the catch movements had improved further.

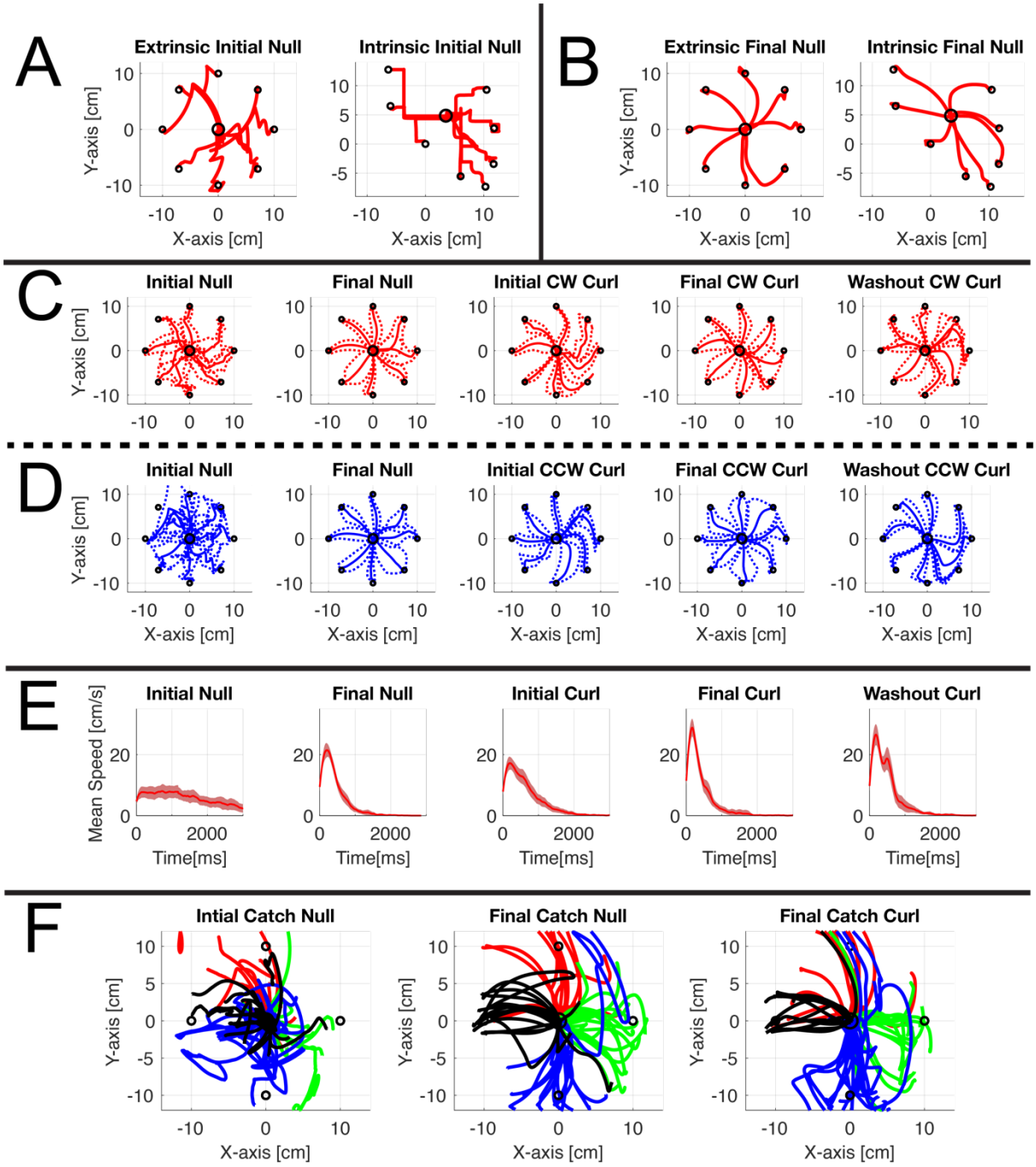

Figure 2. Trajectory plots for Experiment 1 – Kinematic Arm Task. **A:** Representative extrinsic and intrinsic trajectories from the first null trials of an individual participant. **B:** Representative extrinsic and intrinsic trajectories from the last null trials of the same participant. **C:** Mean ± SE extrinsic outward path trajectories for the clockwise (CW) curl field condition during the initial null block, final null block, initial curl block, final curl block, and washout phase blocks. **D:** Corresponding mean ± SE extrinsic outward path trajectories for the counterclockwise (CCW) curl field condition. **E:** Corresponding mean ± SE extrinsic speed profiles across CW and CCW trials. **F:** Extrinsic catch trial trajectories from the first 8 null blocks, the final 8 null blocks, and the final 8 curl blocks. Trajectories to the 0°, 90°, 180°, and 270° targets are plotted in red, green, blue, and black, respectively.

Trajectory Plots Endpoint Mass Task Experiment 2

Fig. 3 shows trajectory plots from Experiment 2 (Endpoint Mass Task), which mirror trends observed in Figure 2 from Experiment 1 (Kinematic Arm Task).

Fig. 3A displays the outward extrinsic and intrinsic trajectories during the initial null phase for a typical participant. As in Experiment 1, extrinsic paths were initially erratic, whereas intrinsic movements showed segmented, independent control of the two input dimensions.

Fig. 3B shows the final null block, where extrinsic trajectories became straighter and intrinsic hand movements continuous and coordinated.

Fig. 3C and Fig. 3D show the mean ± SE extrinsic outward trajectories across participants in the clockwise (CW) and counterclockwise (CCW) conditions, respectively. Movements initially deviated significantly from the straight-line paths but straightened by the end of the null phase. Introduction of the curl field led to systematic curvature, which diminished with adaptation. Upon washout, typical after-effects emerged, showing curvature opposite to the field direction.

Fig. 3E presents mean ± SE speed profiles for extrinsic movements. Early movements were slow and flat-topped profiles; by the end of the null phase, a clear single peak resembling minimum-jerk profile emerged, though still somewhat asymmetric. The curl field initially reduced peak speed and skewed the profile, but symmetry and peak velocity improved by the end of exposure. Wash-out produced more variable speed profiles.

Fig. 3F shows catch trial trajectories from individual participants at the start of the experiment, end of null training, and end of curl field training. As in Experiment 1, early catch movements were often misdirected or poorly scaled. With training, both direction and movement length improved, reflecting better feedforward control of the virtual arm.

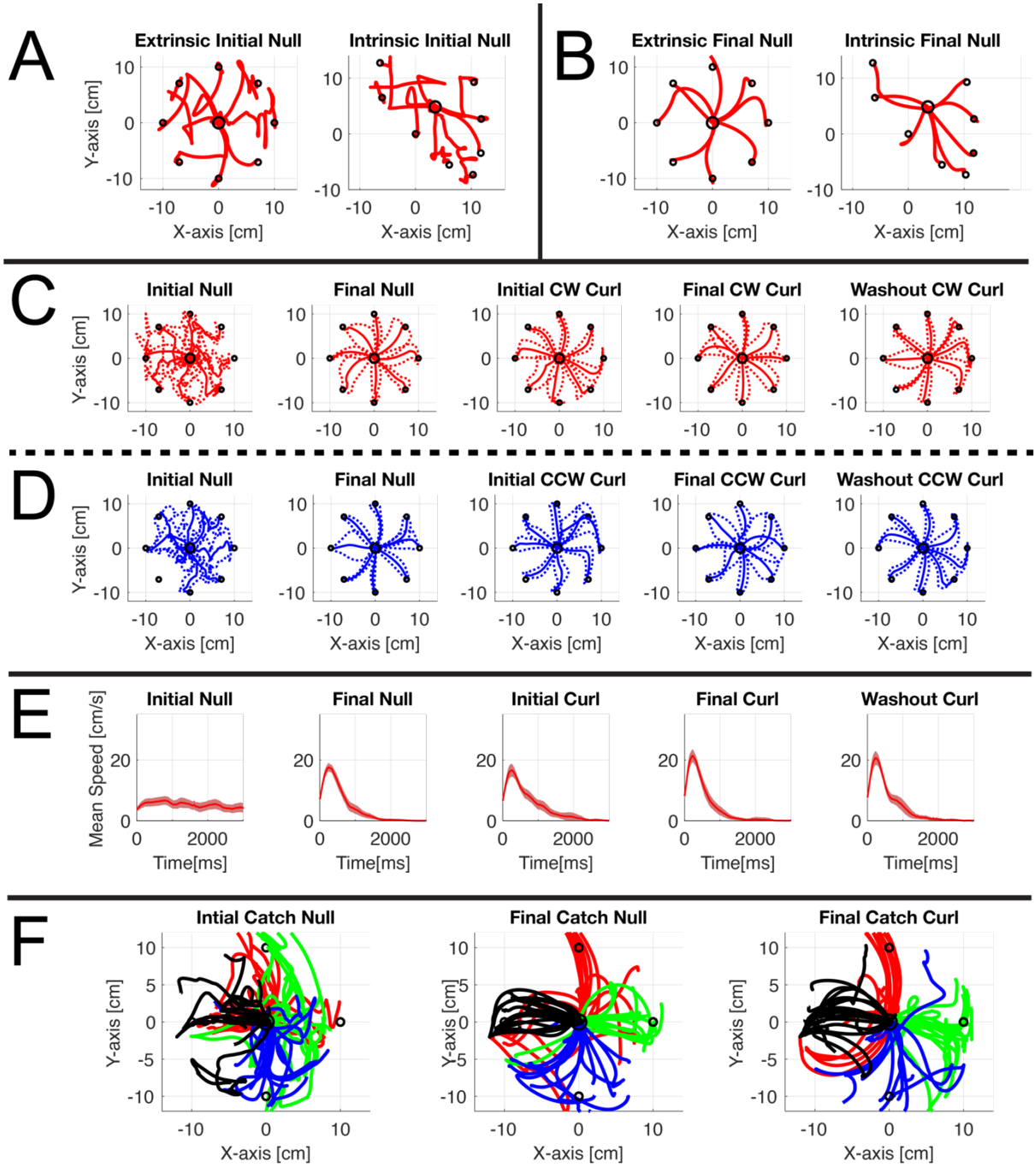

Figure 3. Trajectory plots for Experiment 2 – Endpoint Mass Task. **A:** Representative extrinsic and intrinsic trajectories from the first null trials of an individual participant. **B:** Representative extrinsic and intrinsic trajectories from the last null trials of the same participant. **C:** Mean ± SE extrinsic outward path trajectories for the CW curl field condition. **D:** Mean ± SE extrinsic outward path trajectories for the CCW curl field condition. **E:** Mean ± SE extrinsic speed across CW and CCW trials. **F:** Extrinsic catch trial trajectories for the first 8 null blocks, the final 8 null blocks, and the final 8 curl blocks. Trajectories to the 0°, 90°, 180°, and 270° targets are plotted in red, green, blue, and black, respectively.

Examining Effects within Experiments

We quantified movement trajectory quality with four metrics, AMPE, SMPE, movement duration, and path length, first averaging values across each pair of trial blocks (32 trials per pair). The mean ± SE values of each metric across participants are plotted in Fig. 4. Since experiments ran over two separate sessions, we noted a slight discontinuity in metrics at the start of the second session.

To check for significance within each experimental condition, we compared the metrics at the start of the experiment (initial null phase), at the end of the arm control training phase (final null phase), at the onset of curl field exposure (initial curl phase), at the end of curl field exposure (final curl phase), and finally during the curl field washout (washout phase).

Movement Metrics Plots Experiment 1

The AMPE values are plotted in Fig. 4A in blue. Repeated measures ANOVAs indicated that AMPE showed significant variations between the initial null**,** final null**,** initial curl**,** final curl, and washout phases. Post-hoc comparisons further tested the significant differences between these phases. In this experimental condition ($F = 11.366$; $p < 0.001$; $\omega^2 = 0.463$), AMPE was high at the initial null phase**,** but it significantly reduced by the final null phase ($p_{bonf} = 0.027$). Upon introduction of the curl field in the initial curl phase, it significantly increased ($p_{bonf} < 0.001$). By the final curl phase, AMPE significantly decreased ($p_{bonf} = 0.043$). At the washout phase, AMPE showed a significant difference compared to the final curl phase ($p_{bonf} = 0.047$).

The SMPE values are plotted in Fig. 4B in blue. Repeated measures ANOVAs indicated that SMPE showed significant variations between the initial null, final null, initial curl, final curl, and washout phases. Post-hoc comparisons further tested the significant differences between these phases. In the experimental condition ($F = 26.061$; $p < 0.001$; $\omega^2 = 0.617$), SMPE was highest at the initial null phase, but did not significantly reduce by the final null phase ($p_{bonf} =1.000$). Upon introduction of the curl field in the initial curl phase, it significantly increased ($p_{bonf} < 0.001$). By the final curl phase, SMPE significantly decreased in a fashion typical of that seen in normal curl field exposure experiments. ($p_{bonf} = 0.049$). SMPE at the washout phase showed a significant difference compared to the final curl phase ($p_{bonf} = 0.002$).

The movement duration is plotted in Fig. 4C in blue. Repeated measures ANOVAs indicated that movement duration showed significant variations between the initial null, final null, initial curl, final curl, and washout phases. Post-hoc comparisons further tested the significant differences between these phases. In the experimental condition ($F = 30.213$; $p < 0.001$; $\omega^2 = 0.728$**),** Duration was high at the initial null phase, but it significantly reduced by the final null phase ($p_{bonf} = 0.006$). **U**pon introduction of the curl field in the initial curl phase, it significantly increased **(**$p_{bonf} = 0.009$). By the final curl phase, movement duration significantly decreased ($p_{bonf} = 0.029$). Movement duration at the washout phase showed no significant difference compared to the final curl phase ($p_{bonf} = 0.639$).

Extrinsic path length is plotted in Fig. 4D in blue. Repeated measures ANOVAs indicated that path length showed significant variations between the initial null, final null, initial curl, final curl, and washout phases. Post-hoc comparisons further tested the significant differences between these phases. In the experimental condition ($F = 11.269$; $p < 0.001$; $\omega^2 = 0.466$), path length was high at the initial **null** phase, but it did not significantly reduce by the final null phase ($p_{bonf} = 0.061$). Upon introduction of the curl field in the initial curl phase**,** it significantly increased ($p_{bonf} < 0.001$). By the final curl phase, path length significantly decreased ($p_{bonf} = 0.008$). Path length at the washout phase showed a significant difference compared to the final curl phase ($p_{bonf} = 0.044$).

Movement Metrics Plots Experiment 2

Fig. 4A green plot shows the absolute maximum perpendicular error (AMPE). Repeated measures ANOVAs indicated that AMPE showed significant variations between the initial null**,** final null**,** initial curl**,** final curl**,** and washout phases. Post-hoc comparisons further tested the significant differences between these phases. In the experimental condition ($F = 23.674$; $p < 0.001$; $\omega^2 = 0.629$), AMPE was high at the initial null phase, but it significantly reduced by the final null phase ($p_{bonf} = 0.014$). Upon introduction of the curl field in the initial curl phase**,** it significantly increased ($p_{bonf} < 0.001$). By the final curl phase, AMPE significantly decreased ($p_{bonf} = 0.004$). AMPE at the washout phase showed a significant difference compared to the final curl phase ($p_{bonf} = 0.004$).

Fig. 4B green plot shows the signed maximum perpendicular error (SMPE). Repeated measures ANOVAs indicated that SMPE showed significant variations between the initial null**,** final null**,** initial curl**,** final curl**,** and washout phases. Post-hoc comparisons further tested the significant differences between these phases. In the experimental condition ($F = 14.013$; $p < 0.001$; $\omega^2 = 0.504$), SMPE was highest at the initial null phase, but did not significantly reduce by the final null phase ($p_{bonf} = 1.000$). Upon introduction of the curl field in the initial curl phase**,** it significantly increased ($p_{bonf} = 0.003$). By the final curl phase, SMPE significantly decreased ($p_{bonf} = 0.013$). SMPE at the washout phase showed a significant difference compared to the final curl phase ($p_{bonf} < 0.001$).

The movement duration is plotted in Fig. 4C in green. Repeated measures ANOVAs indicated that movement duration showed significant variations between the initial null, final null, initial curl, final curl, and washout phases. Post-hoc comparisons further tested the significant differences between these phases. In the experimental condition ($F = 166.581$; $p < 0.001$; $\omega^2 = 0.923$**),** Duration was high at the initial null phase, but it significantly reduced by the final null phase ($p_{bonf} < 0.001$). Upon introduction of the curl field in the initial curl phase, it significantly increased **(**$p_{bonf} = 0.016$). By the final curl phase, movement duration significantly decreased ($p_{bonf} < 0.001$). Movement duration at the washout phase showed a significant difference compared to the final curl phase ($p_{bonf} = 0.031$).

Fig. 4D green plot displays movement path length. Repeated measures ANOVAs indicated that path length showed significant variations between the initial null**,** final null**,** initial curl**,** final curl**,** and washout phases. Post-hoc comparisons further tested the significant differences between these phases. In the experimental condition ($F = 23.558$; $p < 0.001$; $\omega^2 = 0.647$), path length was high at the initial null phase, but it did significantly reduce by the final null phase ($p_{bonf} = 0.013$). Upon introduction of the curl field in the initial curl phase**,** it significantly increased ($p_{bonf} < 0.001$). By the final curl phase, path length significantly decreased ($p_{bonf} = 0.009$). Path length at the washout phase showed a significant difference compared to the final curl phase ($p_{bonf} = 0.020$).

Comparison of Metrics Across Experiments

To compare the two experimental conditions, we plotted the four metrics AMPE, SMPE, duration and path length against block pairs, as shown in Fig. 4. In addition, we ran ANOVAs analysis to compare metrics computed over 10 blocks (160 trials) at the end of the kinematic learning, at the start curl field exposure, and at the last curl field exposure phases between Kinematic Arm Experiment 1 and the Endpoint Mass Experiment 2.

Fig. 4A shows absolute MPE (AMPE) decreases in both experimental conditions. The last null phase showed a significant variation across experimental conditions ($F = 4.778$; $p = 0.046$; $\omega^2 = 0.191$). The first curl phase showed a significant variation across experimental conditions ($F = 15.405$; $p = 0.002$; $\omega^2 = 0.474$). Post-hoc comparisons revealed a significant difference ($p = 0.002$). The final curl phase showed a significant variation across experimental conditions ($F = 8.492$; $p = 0.011$; $\omega^2 = 0.319$). Throughout training, the use of an endpoint mass consistently results in lower AMPE values than those observed in the kinematic arm condition. Notably, at the end of the null field phase, AMPE had decayed to a lower value in the mass condition. When the curl field was introduced, AMPE rose again in both experimental conditions. However, the kinematic arm condition showed a higher overall AMPE compared to the mass condition.

Fig. 4B shows the trajectory signed MPE (SMPE) plotted against pairs of trial blocks. The last null phase showed no significant variation across experimental conditions ($F = 0.176$; $p = 0.681$; $\omega^2 = 0.000$). The first curl phase showed a significant variation across experimental conditions ($F = 32.405$; $p < 0.001$; $\omega^2 = 0.662$). Post-hoc comparisons revealed a significant difference ($p < 0.001$). The final curl phases

showed a significant variation across experimental conditions ($F = 9.015$; $p = 0.010$; $\omega^2 = 0.334$).

When no curl field is present, the signed MPE value indicates little bias in movement trajectories. Consequently, in both training conditions, with and without the endpoint mass, the SMPE values remain close to the zero baseline. However, upon introduction of the curl field, there is a dramatic increase in SMPE in both conditions. In the kinematic arm condition, this value exhibited a slower decay and maintained a large offset bias. In contrast, the endpoint mass condition shows a rapid decay in SMPE, returning closer to the baseline value. In both conditions, expected washout effects are observed, with SMPE values changing sign, indicating that predictive compensation to the novel curl field dynamics had developed.

Fig. 4C shows the movement duration across pairs of trial blocks over the experiments. The last null phase showed a significant variation across experimental conditions ($F = 18.603$; $p < 0.001$; $\omega^2 = 0.524$). The first curl phase showed a significant variation across experimental conditions ($F = 6.952$; $p = 0.020$; $\omega^2 = 0.271$). The final curl phase showed no significant variation across experimental conditions ($F = 2.218$; $p = 0.159$; $\omega^2 = 0.071$). Thus, movement durations are generally shorter in the kinematic arm condition, suggesting participants move more slowly when performing the endpoint mass task.

Fig. 4D shows the extrinsic trajectory length over pairs of trial blocks over the experiments. The last null phase showed no significant variations across experimental conditions ($F = 1.171$; $p =0.441$; $\omega^2 = 0.070$). The first curl phase showed no significant variation across experimental conditions ($F = 0.965$; $p = 0.512$; $\omega^2 = 0.000$). The final curl phase showed no significant variation across experimental conditions ($F = 0.830$; $p = 0.591$; $\omega^2 = 0.000$).

To summarize the main results, by the end of the kinematic learning phase, training with haptic feedback in the endpoint mass condition resulted in significantly straighter movements than in the purely kinematic condition, as indicated by lower AMPE values. In addition, the endpoint mass condition led to straighter movements at the onset of curl field exposure and greater adaptation by the end of the curl field exposure phase. This was reflected in both AMPE and SMPE measurements. The duration of movements was significantly longer in the endpoint mass condition; however, the path length did not differ significantly.

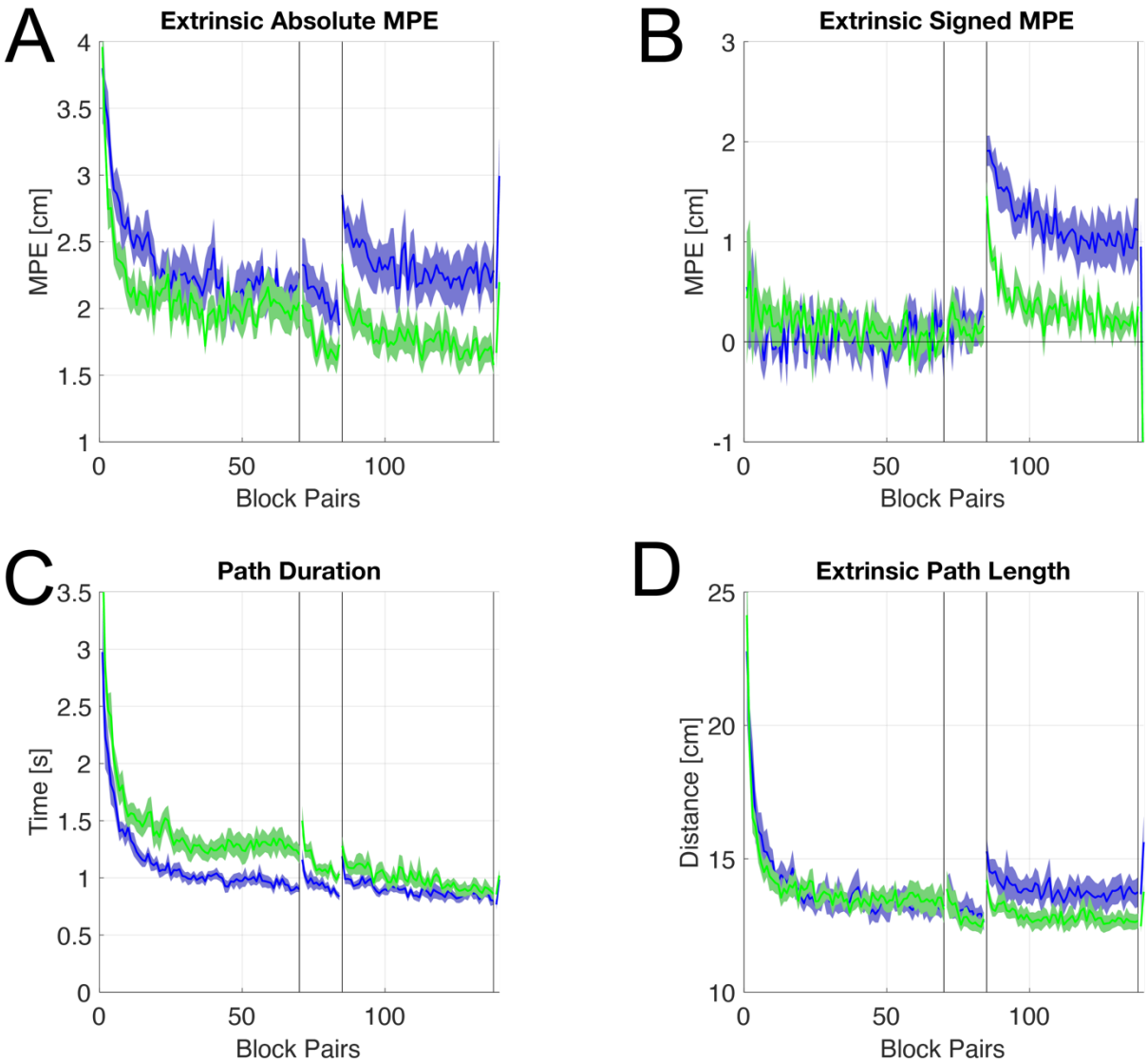

Figure 4. Comparison Movement metrics between Experiment 1 – Kinematic Arm (blue) and Experiment 2 – Endpoint Mass Task (green). **A:** Mean ± SE extrinsic absolute MPE shown over the experiments. **B:** Mean ± SE signed extrinsic MPE over the experiments. **C:** Mean ± SE trial duration over the experiments. **D:** Mean ± SE extrinsic path length over the experiments.

Discussion (1339/1500)

Summary

This study demonstrates that augmenting practice with haptic force feedback from a simulated endpoint mass facilitates the de novo learning of arm kinematics and dynamics in a virtual 2D environment. Although both groups of participants initially exhibited similar learning trajectories, those who trained with the simulated mass ultimately achieved greater inter-limb coordination and increased extrinsic trajectory linearity over time.

In the Kinematic Task (Experiment 1), participants initially moved their hands sequentially, briefly arresting one hand before advancing the other. However, they soon adopted simultaneous bimanual movements and extrinsic trajectories progressively straightened with practice. Upon introduction of a curl field, trajectories initially showed pronounced curvature, but these straightened with continued exposure, similar to typical behavior observed in curl field learning. However, observation of the signed MPE suggested that adaptation was incomplete by the end of the curl field exposure.

The Endpoint Mass Task (Experiment 2), which added a 2 kg end point mass, displayed parallel trends. Early movements again featured hand control, but the simulated inertia induced noticeable overshoot. As training progressed, they quickly adopted simultaneous movements and gradually learned to control the arm to perform point-to-point movements, again resulting in straighter extrinsic trajectories with practice. Upon introduction of the curl field, loopy trajectories were again observed, though to a lesser extent than in Experiment 1, and the signed MPE was considerably lower. The systematic bias seen in Experiment 1 was absent and signed MPE values had nearly returned to baseline by the end of curl field exposure.

Crucially, when exposed to a novel dynamic perturbation (curl field), robust adaptation emerged exclusively in the force-feedback group, likely because prior exposure to endpoint force control and reduced trajectory biases. These findings suggest that experiencing physical forces during training enriches internal models used for motor control, enabling more robust generalization to new dynamic contexts. This has important implications for the design of training protocols in rehabilitation, robotics, and skilled tool use, where incorporating force feedback could accelerate and deepen motor learning.

Stereotypical Behaviors

Human point-to-point reaching movements exhibit stereotyped kinematic regularities. Work examining hand movements has consistently shown that participants exhibit specific invariant features [15,32–35]: These include (i) bell-shaped velocity profiles [36], (ii) distinct acceleration and deceleration phases [37,38]; and (iii) trajectories that are predominantly straight [39], although slight curvature may be observed depending on workspace geometry [40,41].

We observed comparable characteristics in extrinsic trajectories of the virtual arm endpoint: paths progressively straightened with practice, and the corresponding speed profiles became increasingly symmetric and bell-shaped. The former phenomenon has also been previously reported in brain–machine-interface (BMI) tasks when visual feedback of movement is available [21].

Another aspect of our experiments reveals how participants explored the novel kinematics during the early stages of de novo learning. In developmental robotics, exploratory behaviors such as babbling have been used to develop transformations between coordinate frames [42], and to learn control [43]. Extending this idea, goal babbling has been proposed as a method for learning the inverse kinematics of robotic arms [44,45], where exploration is directed toward achieving desired outcomes. Similarly,

goal-directed feedback has been shown to facilitate skill learning in humans [46]. In our study, participants appeared to engage in a form of goal-directed exploration, using feedback to iteratively refine their understanding of the novel kinematic transformations.

Haptic Feedback and Networks in the Brain

Proprioceptive acuity training has been shown to enhance motor learning [47]. Haptic feedback likely facilitates de novo motor learning by providing rich proprioceptive and tactile information. This may enhance the engagement of distributed neural networks, including the cerebellum for predictive modeling and internal model formation [48,49], the somatosensory and parietal cortices for integrating haptic input and updating limb representations [50,51], and motor areas for encoding novel dynamics and motor skill acquisition [52,53]. Importantly, de novo learning appears to recruit a broader set of neural circuits compared to traditional adaptation tasks, reflecting the need to construct entirely new control policies rather than merely modifying existing ones.

While cerebellar circuits are heavily implicated in adaptation through the computation of sensory prediction errors [49,54], de novo learning engages additional regions such as the basal ganglia and prefrontal cortex [55–57]. The basal ganglia support reinforcement learning processes essential for selecting successful movement strategies, whereas the prefrontal cortex facilitates the maintenance and flexible updating of new sensorimotor mappings, particularly during the exploratory phases of learning [58,59]. As learning progresses, gradual reorganization within sensorimotor areas, including the primary motor cortex (M1) and premotor regions, consolidates novel control policies into more automatic motor programs [60,61]. Together, the engagement of this distributed network underscores the complexity of de novo skill acquisition and highlights the interplay between error-driven, reinforcement-based, and strategic processes necessary for building new action-outcome associations.

De Novo Learning

The relative ease with which we can learn novel tasks, even those involving almost arbitrary kinematics and dynamics, suggests that the motor system inherently possesses the ability to perform system identification and develop adaptive control strategies. This capability is not confined to the kinematics and dynamics of our own bodies. We are also proficient at learning how to use extensions of our bodies, like simple tools such as hammers, spanners, and screwdrivers. Moreover, we can attain mastery over more complex systems, such as driving a car or operating an excavator. This latter example closely resembles the scenario investigated here, namely learning to control a novel arm.

When encountering a new motor task with an unfamiliar muscle-to-movement mapping, predictive motor commands cannot be generated due to the absence of prior knowledge. Consequently, exploring muscle activity space becomes essential to learn this relationship. It is enlightening to observe how this situation mirrors the developmental challenges faced by infants in learning goal-directed reaching [62–64] and how it relates to our novel arm task. Learning requires the ability to evaluate actions

and improve strategies, heavily relying on visual feedback, while haptic feedback also plays a valuable role.

Motor skill acquisition [65,66] involves the improvement of movement and task performance through practice [67]. This process ranges from simple adaptation to changes in kinematics or dynamics. Early research quantified the nature of arm kinematics and dynamics [33]. Subsequent studies have furthered our understanding of how the motor system learns to navigate unfamiliar environments. For instance, research on de novo learning has investigated how individuals adapt their motor skills to map and manipulate new spatial contexts [68]. In their study, participants learned to control a cursor through coordinated movements and developed a mental representation of Euclidean space for remapping hand movements. Training with terminal visual feedback resulted in smoother cursor trajectories and reduced unnecessary movements in non-critical degrees of freedom. Notably, full visual feedback accelerated the learning process.

A study using a novel visuomotor task investigated the mapping between isometric bimanual actions and the control of a cursor in 3D. Participants exhibited distinct stages in their behaviors [35]. Similarly, it is enlightening to see how patients adapt with artificial limbs [69]. Electromyogram signals have been used to control cursor movements [70] or a virtual mass [71]. Neural signals have also been used to control cursor movements [72], as well as prosthetic devices [73].

Brain-Machine Interfaces (BMIs) are often studied as a means to control prosthetic limbs [74] and have broadened the scope of research from simple adaptations to more substantial changes in dynamics and vision, as well as enhancing our understanding of neural representations [75,76].

Although not investigated here, as well as using point-to-point movement tasks, "de novo" learning has been examined in the continuous control of tracking under rotation and mirror reversal of visual feedback [24]. This was followed by investigations into the influence of noise and the estimation of sensitivity derivatives in "de novo" learning [77].

A comprehensive study of long-term "de novo" bimanual learning was also undertaken, highlighting the long timescale needed to achieve baseline performance [25]. The process of learning "de novo" control becomes habitual [78]. More recently, neural network models (specifically recurrent neural networks, RNNs), have been investigated to examine "de novo" learning [79], providing a new modeling paradigm to investigate and explain human sensorimotor control.

Author Contributions

ISH conceived, designed, and implemented the current study. LAH conducted data collection. Data analysis was carried out by ISH. The initial draft of the manuscript was written by ISH. Both authors (ISH and LAH) reviewed and edited the manuscript.

Competing Interest Statement

The authors declare that they have no financial, personal, or professional interests that could be construed to have influenced the paper.

References

1. Savion-Lemieux, T. & Penhune, V. B. The effects of practice and delay on motor skill learning and retention. *Exp Brain Res* **161**, 423–431 (2005).
2. Reis, J. *et al.* Noninvasive cortical stimulation enhances motor skill acquisition over multiple days through an effect on consolidation. *Proceedings of the National Academy of Sciences* **106**, 1590–1595 (2009).
3. Shmuelof, L., Krakauer, J. W. & Mazzoni, P. How is a motor skill learned? Change and invariance at the levels of task success and trajectory control. *Journal of Neurophysiology* **108**, 578–594 (2012).
4. Krakauer, J. W., Hadjiosif, A. M., Xu, J., Wong, A. L. & Haith, A. M. Motor learning. *Compr Physiol* **9**, 613–663 (2019).
5. Krakauer, J. W., Pine, Z. M., Ghilardi, M. F. & Ghez, C. Learning of visuomotor transformations for vectorial planning of reaching trajectories. *The Journal of neuroscience : the official journal of the Society for Neuroscience* **20**, 8916–8924 (2000).
6. Krakauer, J. W., Ghez, C. & Ghilardi, M. F. Adaptation to visuomotor transformations: consolidation, interference, and forgetting. *The Journal of neuroscience : the official journal of the Society for Neuroscience* **25**, 473–478 (2005).
7. Bock, O., Schneider, S. & Bloomberg, J. Conditions for interference versus facilitation during sequential sensorimotor adaptation. *Experimental Brain Research* **138**, 359–365 (2001).

8. Goedert, K. M. & Willingham, D. B. Patterns of Interference in Sequence Learning and Prism Adaptation Inconsistent With the Consolidation Hypothesis. *Learn. Mem.* **9**, 279–292 (2002).
9. Lackner, J. R. & Dizio, P. Rapid adaptation to Coriolis force perturbations of arm trajectory. *J Neurophysiol* **72**, 299–313 (1994).
10. Shadmehr, R. & Mussa-Ivaldi, F. A. Adaptive representation of dynamics during learning of a motor task. *J. Neurosci.* **14**, 3208–3224 (1994).
11. Brashers-Krug, T., Shadmehr, R. & Bizzi, E. Consolidation in human motor memory. *Nature* **382**, 252–255 (1996).
12. Gandolfo, F., Mussa-Ivaldi, F. A. & Bizzi, E. Motor learning by field approximation. *PNAS* **93**, 3843–3846 (1996).
13. Flanagan, J. R. *et al.* Composition and decomposition of internal models in motor learning under altered kinematic and dynamic environments. *The Journal of neuroscience : the official journal of the Society for Neuroscience* **19**, RC34 (1999).
14. Krakauer, J. W., Ghilardi, M. F. & Ghez, C. Independent learning of internal models for kinematic and dynamic control of reaching. *Nature Neuroscience* **2**, 1026–1031 (1999).
15. Flanagan, J. R. & Rao, A. K. Trajectory adaptation to a nonlinear visuomotor transformation: evidence of motion planning in visually perceived space. *Journal of neurophysiology* **74**, 2174–2178 (1995).
16. Lillicrap, T. P. *et al.* Adapting to inversion of the visual field: a new twist on an old problem. *Exp Brain Res* **228**, 327–339 (2013).
17. Telgen, S., Parvin, D. & Diedrichsen, J. Mirror reversal and visual rotation are learned and consolidated via separate mechanisms: recalibrating or learning de novo? *Journal of Neuroscience* **34**, 13768–13779 (2014).

18. Pouget, A., Fisher, S. & Sejnowski, T. J. Hierarchical Transformation of Space in the Visual System. in *Advances in Neural Information Processing Systems* vol. 4 (Morgan-Kaufmann, 1991).
19. Pouget, A. & Snyder, L. H. Computational approaches to sensorimotor transformations. *Nature Neuroscience* **3 Suppl**, 1192–1198 (2000).
20. Danziger*, Z., Fishbach, A. & Mussa-Ivaldi, F. A. Learning Algorithms for Human–Machine Interfaces. *IEEE Transactions on Biomedical Engineering* **56**, 1502–1511 (2009).
21. Danziger, Z. & Mussa-Ivaldi, F. A. The Influence of Visual Motion on Motor Learning. *J. Neurosci.* **32**, 9859–9869 (2012).
22. Liu, X., Mosier, K. M., Mussa-Ivaldi, F. A., Casadio, M. & Scheidt, R. A. Reorganization of Finger Coordination Patterns During Adaptation to Rotation and Scaling of a Newly Learned Sensorimotor Transformation. *Journal of Neurophysiology* **105**, 454–473 (2011).
23. Sternad, D. It's not (only) the mean that matters: variability, noise and exploration in skill learning. *Current Opinion in Behavioral Sciences* **20**, 183–195 (2018).
24. Yang, C. S., Cowan, N. J. & Haith, A. M. De novo learning versus adaptation of continuous control in a manual tracking task. *eLife* **10**, e62578 (2021).
25. Haith, A. M., Yang, C. S., Pakpoor, J. & Kita, K. De novo motor learning of a bimanual control task over multiple days of practice. *Journal of Neurophysiology* **128**, 982–993 (2022).
26. Oldfield, R. C. The assessment and analysis of handedness: The Edinburgh inventory. *Neuropsychologia* **9**, 97–113 (1971).
27. Galvin, J. E., Tolea, M. I., Rosenfeld, A. & Chrisphonte, S. The Quick Physical Activity Rating (QPAR) scale: A brief assessment of physical activity in older adults with and without cognitive impairment. *PLOS ONE* **15**, e0241641 (2020).

28. Howard, I. S., Ingram, J. N. & Wolpert, D. M. A modular planar robotic manipulandum with end-point torque control. *J Neurosci Meth* **181**, 199–211 (2009).
29. Scheidt, R. A., Reinkensmeyer, D. J., Conditt, M. A., Rymer, W. Z. & Mussa-Ivaldi, F. A. Persistence of motor adaptation during constrained, multi-joint, arm movements. *J Neurophysiol* **84**, 853–862 (2000).
30. Smith, M. A., Ghazizadeh, A. & Shadmehr, R. Interacting adaptive processes with different timescales underlie short-term motor learning. *PLoS Biology* **4**, e179 (2006).
31. JASP Team, Version 0.19.1. JASP. (2024).
32. Morasso, P. Spatial control of arm movements. *Exp Brain Res* **42**, 223–227 (1981).
33. Atkeson, C. G. LEARNING ARM KINEMATICS AND DYNAMICS. *Annual Review of Neuroscience* **12**, 157–183 (1989).
34. Burdet, E. & Milner, T. E. Quantization of human motions and learning of accurate movements. *Biological cybernetics* **78**, 307–318 (1998).
35. Sailer, U., Flanagan, J. R. & Johansson, R. S. Eye-hand coordination during learning of a novel visuomotor task. *Journal of Neuroscience* **25**, 8833–8842 (2005).
36. Flash, T. & Hogan, N. The coordination of arm movements: an experimentally confirmed mathematical model. *J. Neurosci.* **5**, 1688–1703 (1985).
37. Soechting, J. F. & Lacquaniti, F. Invariant characteristics of a pointing movement in man. *Journal of Neuroscience* **1**, 710–720 (1981).
38. Gottlieb, G. L. Muscle Activation Patterns During Two Types of Voluntary Single-Joint Movement. *Journal of Neurophysiology* **80**, 1860–1867 (1998).
39. Abend, W., Bizzi, E. & Morasso, P. Human arm trajectory formation. *Brain* **105**, 331–348 (1982).

40. Atkeson, C. G. & Hollerbach, J. M. Kinematic features of unrestrained vertical arm movements. *J. Neurosci.* **5**, 2318–2330 (1985).

41. Boessenkool, J. J., Nijhof, E.-J. & Erkelens, C. J. A comparison of curvatures of left and right hand movements in a simple pointing task. *Exp Brain Res* **120**, 369–376 (1998).

42. Fiala, J. C. A network for learning kinematics with application to human reaching models. in *Proceedings of 1994 IEEE International Conference on Neural Networks (ICNN'94)* vol. 5 2759–2764 vol.5 (1994).

43. Demiris, Y. & Dearden, A. From motor babbling to hierarchical learning by imitation: a robot developmental pathway. in (eds. Berthouze, L. et al.) vol. 123 31–37 (Lund University Cognitive Studies, 2005).

44. Rolf, M., Steil, J. J. & Gienger, M. Goal Babbling Permits Direct Learning of Inverse Kinematics. *IEEE Transactions on Autonomous Mental Development* **2**, 216–229 (2010).

45. Rolf, M. & Steil, J. J. Efficient Exploratory Learning of Inverse Kinematics on a Bionic Elephant Trunk. *IEEE Transactions on Neural Networks and Learning Systems* **25**, 1147–1160 (2014).

46. Rohde, M., Narioka, K., Steil, J. J., Klein, L. K. & Ernst, M. O. Goal-related feedback guides motor exploration and redundancy resolution in human motor skill acquisition. *PLOS Computational Biology* **15**, e1006676 (2019).

47. Wong, J. D., Kistemaker, D. A., Chin, A. & Gribble, P. L. Can proprioceptive training improve motor learning? *J Neurophysiol* **108**, 3313–3321 (2012).

48. Shadmehr, R. & Krakauer, J. W. A computational neuroanatomy for motor control. *Experimental brain research* **185**, 359–381 (2008).

49. Izawa, J. & Shadmehr, R. Learning from sensory and reward prediction errors during motor adaptation. *PLoS computational biology* **7**, e1002012 (2011).

50. Wolpert, D. M., Goodbody, S. J. & Husain, M. Maintaining internal representations: the role of the human superior parietal lobe. *Nature Neuroscience* **1**, 529–533 (1998).
51. Diedrichsen, J., Hashambhoy, Y., Rane, T. & Shadmehr, R. Neural correlates of reach errors. *Journal of Neuroscience* **25**, 9919–9931 (2005).
52. Sanes, J. N. & Donoghue, J. P. Plasticity and Primary Motor Cortex. *Annual Review of Neuroscience* **23**, 393–415 (2000).
53. Galea, J. M. J., Vazquez, A. A., Pasricha, N. N., de Xivry, J.-J. O. J. & Celnik, P. P. Dissociating the roles of the cerebellum and motor cortex during adaptive learning: the motor cortex retains what the cerebellum learns. *Cerebral cortex (New York, N.Y. : 1991)* **21**, 1761–1770 (2011).
54. Tseng, Y.-W., Diedrichsen, J., Krakauer, J. W., Shadmehr, R. & Bastian, A. J. Sensory prediction errors drive cerebellum-dependent adaptation of reaching. *Journal of neurophysiology* **98**, 54–62 (2007).
55. Doyon, J. *et al.* Contributions of the basal ganglia and functionally related brain structures to motor learning. *Behav Brain Res* **199**, 61–75 (2009).
56. Hardwick, R. M., Rottschy, C., Miall, R. C. & Eickhoff, S. B. A quantitative meta-analysis and review of motor learning in the human brain. *Neuroimage* **67**, 283–297 (2013).
57. Dhawale, A. K., Smith, M. A. & Ölveczky, B. P. The Role of Variability in Motor Learning. *Annu Rev Neurosci* **40**, 479–498 (2017).
58. Taylor, J. A. & Ivry, R. B. Cerebellar and prefrontal cortex contributions to adaptation, strategies, and reinforcement learning. *Progress in brain research* **210**, 217–53 (2014).
59. Haith, A. M. & Krakauer, J. W. The multiple effects of practice: skill, habit and reduced cognitive load. *Curr Opin Behav Sci* **20**, 196–201 (2018).

60. Mawase, F., Lopez, D., Celnik, P. A. & Haith, A. M. Movement Repetition Facilitates Response Preparation. *Cell Rep* **24**, 801–808 (2018).

61. Yokoi, A. & Diedrichsen, J. Neural Organization of Hierarchical Motor Sequence Representations in the Human Neocortex. *Neuron* **103**, 1178-1190.e7 (2019).

62. von Hofsten, C. Developmental changes in the organization of prereaching movements. *Developmental Psychology* **20**, 378–388 (1984).

63. Konczak, J., Borutta, M., Topka, H. & Dichgans, J. The development of goal-directed reaching in infants: hand trajectory formation and joint torque control. *Exp Brain Res* **106**, (1995).

64. Konczak, J. & Dichgans, J. The Development of Hand Trajectory Formation and Joint Kinematics During Reaching in Infancy. in *Three-dimensional Kinematics of the Eye, Head and Limb Movements* (Routledge, 1997).

65. Schmidt, R. A. A schema theory of discrete motor skill learning. *Psychological Review* **82**, 225–260 (1975).

66. Newell, K. M. Motor Skill Acquisition. *Annual Review of Psychology* **42**, 213–237 (1991).

67. Willingham, D. B. A neuropsychological theory of motor skill learning. *Psychological Review* **105**, 558–584 (1998).

68. Mosier, K. M., Scheidt, R. A., Acosta, S. & Mussa-Ivaldi, F. A. Remapping hand movements in a novel geometrical environment. *Journal of neurophysiology* **94**, 4362–4372 (2005).

69. Maimon-Mor, R. O., Schone, H. R., Henderson Slater, D., Faisal, A. A. & Makin, T. R. Early life experience sets hard limits on motor learning as evidenced from artificial arm use. *eLife* **10**, e66320 (2021).

70. Radhakrishnan, S. M., Baker, S. N. & Jackson, A. Learning a Novel Myoelectric-Controlled Interface Task. *Journal of Neurophysiology* **100**, 2397–2408 (2008).

71. Berger, D. J., Gentner, R., Edmunds, T., Pai, D. K. & D'Avella, A. Differences in Adaptation Rates after Virtual Surgeries Provide Direct Evidence for Modularity. *Journal of Neuroscience* **33**, 12384–12394 (2013).
72. Oby, E. R. *et al.* New neural activity patterns emerge with long-term learning. *Proceedings of the National Academy of Sciences* **116**, 15210–15215 (2019).
73. Ganguly, K. & Carmena, J. M. Emergence of a Stable Cortical Map for Neuroprosthetic Control. *PLOS Biology* **7**, e1000153 (2009).
74. Casadio, M., Ranganathan, R. & Mussa-Ivaldi, F. A. The Body-Machine Interface: A New Perspective on an Old Theme. *Journal of Motor Behavior* **44**, 419–433 (2012).
75. Orsborn, A. L. *et al.* Closed-Loop Decoder Adaptation Shapes Neural Plasticity for Skillful Neuroprosthetic Control. *Neuron* **82**, 1380–1393 (2014).
76. Sadtler, P. T. *et al.* Neural constraints on learning. *Nature* **512**, 423–426 (2014).
77. Dal'Bello, L. R. & Izawa, J. Computational role of exploration noise in error-based de novo motor learning. *Neural Networks* **153**, 349–372 (2022).
78. Yang, C. S., Cowan, N. J. & Haith, A. M. Control becomes habitual early on when learning a novel motor skill. *Journal of Neurophysiology* **128**, 1278–1291 (2022).
79. Chang, J. C., Perich, M. G., Miller, L. E., Gallego, J. A. & Clopath, C. De novo motor learning creates structure in neural activity that shapes adaptation. *Nat Commun* **15**, 4084 (2024).